

ARTICLES

High-order pair-reduced neural network architecture for global potential energy surface exploration across the periodic table

Zheng-Xin Yang^{1†}, Xin-Tian Xie^{1†}, Zhen-Xiong Wang^{1†}, Dong-Xiao Chen¹, Zi-Xing Guo¹, Jia-Jie Du¹, Qi-Ming Liang¹, Qian-Yu Liu¹, Cheng Shang^{1*} & Zhi-Pan Liu^{1,2*}

¹State Key Laboratory of Porous Materials for Separation and Conversion, Collaborative Innovation Center of Chemistry for Energy Material, Shanghai Key Laboratory of Molecular Catalysis and Innovative Materials, Key Laboratory of Computational Physical Science, Department of Chemistry, Fudan University, Shanghai 200433, China

²State Key Laboratory of Metal Organic Chemistry, Shanghai Institute of Organic Chemistry, Chinese Academy of Sciences, Shanghai 200032, China

[†]Equally contributed to this work.

*Corresponding authors (email: cshang@fudan.edu.cn; zpliu@fudan.edu.cn)

Received 23 September 2025; Accepted 11 October 2025; Published online 11 November 2025

Abstract One universal potential for all-purpose atomic simulations has been pursued for decades, but has faced extreme challenges in both reaching high representation capability of the model and constructing comprehensive potential energy surface (PES) data across the periodic table. Here we present a low-cost and high-accuracy machine learning (ML) model, namely high-order pair-reduced neural network (HPNN), which adopts a hierarchical angular interaction scheme with reduced pair dimension, enabling the incorporation of spherical harmonics up to $l = 6$ at a low cost. Using the architecture, we demonstrate the capability to train a generalized global neural network potential (GG-NN) using a comprehensive dataset of 5.84 million global PES configurations covering 83 elements in the periodic table collected from LASP project in the past decade, which reaches the root-mean-square errors of 7.3 meV/atom for energy and 0.16 eV/Å for force. By benchmarking with mainstream ML models on representative global PESs, *e.g.*, Ti–O and C–H–O, we show the high performance of specially-trained HPNN and GG-NN both in the inference speed and in the accuracy. Our results pave the way to exploit the generalized global potential for large-scale atomic simulations to accelerate molecules and material prediction via global PES exploration.

Keywords atomic simulations, high-order pair-reduced neural network, generalized global neural network, universal potential, reaction barrier prediction

1 Introduction

Over the past decade, machine learning (ML) potentials have revolutionized large-scale atomic simulations by offering a significant speedup in potential energy surface (PES) evaluation while maintaining the high accuracy comparable to quantum mechanics (QM) calculations [1–7]. It benefits particularly the fields requiring long-time simulations, such as molecular dynamics (MD) [8–10] and global PES exploration, aiming to predict the physicochemical properties of materials and reactions [11–13]. However, current ML potentials generally learn from relatively simple datasets dominated by stable local minima [14,15], lacking the structural diversity on the reaction intermediates (transition states), glassy and high-energy minima that are common in global PES data, and thus greatly hamper the predictive power of ML-based atomic simulations [16]. This is partly because of the lack of a global PES dataset for all elements, but, more importantly, the great difficulty in developing a general and reliable ML model that can fit global PES data across the periodic table with high accuracy and high efficiency.

The representation capability of an ML potential depends critically on the dataset to learn and the ML model employed to learn the dataset. The ML model, depending on the choice, can be implemented to suit different hardware platforms, *i.e.*, central processing units (CPUs) and graphics processing units (GPUs)

[6,17]. For ML potentials using explicit function (no learnable parameters) structure descriptors [18] as input (also known as local descriptors), such as global neural network (G-NN) potential implemented in LASP project [19–21] by our group, the high-order (*e.g.*, $l = 6$) spherical functions can be utilized directly to learn complex chemical environment and feasible to implement parallelly in CPU machines. However, these potentials can maximally handle the global PES data with fewer than 10 elements due to the limitation of CPU in training a large dataset (*e.g.*, > 200 K). On the other hand, GPU-machines with massive computation units excel at handling large training datasets and expansive parameter spaces [22–26], *e.g.*, massive learnable parameters in the non-local structure descriptors, holding the promise to achieve better generality and higher accuracy ML models than CPU-machines [27,28]. One major concern with GPU-based ML potentials is how to incorporate the nonlocal and complex spatial information effectively and efficiently.

To date, a standard choice of GPU-based ML models for training potentials [29] is the graph neural network via message-passing, *i.e.*, message passing neural network (MPNN), which represents atoms and bonds as nodes and edges in the graph, respectively, and extracts atomic features via iterative message passing between nodes. It was, however, soon realized that only two-body (pair-wise) distances between neighboring atoms, as first implemented in SchNet [22], cannot capture fine spatial information in structure.

Citation: Yang ZX, Xie XT, Wang ZX, Chen DX, Guo ZX, Du JJ, Liang QM, Liu QY, Shang C, Liu ZP. High-order pair-reduced neural network architecture for global potential energy surface exploration across the periodic table. *Sci China Chem*, <https://doi.org/10.1007/s11426-025-3054-y>

Subsequently, extensive efforts have sought to integrate spatial information into MPNN models to enhance the ML potential accuracy in describing PES [30–32]. The early efforts by incorporating explicit three and four-body functions (angle and torsion information [33]) following those practiced in CPU-based ML potentials [34,35] did show encouraging progress, but these explicit functions significantly hurt the performance in speed on GPU computation [36]. Another idea to include angular spatial information by using spherical harmonics $Y^{l,m}$ with high-order angular moments ($l > 0$), as learning from atomic wave functions [18,37,38]. Equivariant graph neural networks (EGNNs) proposed by Satorras *et al.* [39] and implemented later in PaiNN [40] and ET [24] potentials demonstrate that the incorporation of first-order ($l = 1$) spherical harmonics, equivalent to three-body functions, can already achieve better performance than explicit function potentials. By further increasing angular moment up to $l = 3$ using the Clebsch-Gordan (CG) tensor product formalism to realize the coupling between high-order vectors [41], a group of ML models, such as NequIP [42], Allegro [43], and MACE [44], do achieve the state-of-the-art performance, but, unfortunately, sacrifice significantly the performance in speed because the CG tensor product is a heavy operation of $O(l^6)$ complexity on atomic pairs (N_p) [45], *i.e.*, $O(n \times N_p \times l^6)$ for systems with n atoms. Specifically, Wang *et al.* [46] benchmarked the performance of different ML models on a Chignolin peptide (166 atoms), and showed that MACE [44] potential with only $l = 2$, while more accurate, is about one order of magnitude slower than PaiNN [40] with $l = 1$. Recent years have seen encouraging progress in using higher-order spherical harmonics while reducing the intrinsic scaling, such as SO3KRATES and eSCN models [45,47], which can reduce the spherical-harmonics-related computational complexity to $O(l^2)$ and $O(l^3)$, respectively. Specifically, SO3KRATES separates the invariant and equivariant information to avoid the expensive tensor products on atomic pairs. To date, it remains largely elusive whether the high angular moment, *e.g.*, $l > 2$, is essential to learn a global PES with many elements, and, if it is true, could the computational cost in incorporating such high angular moment spherical harmonics be reduced, considering the huge data to learn global PES of all elements?

Here, we develop a low-cost GPU-based ML model, named the high-order pair-reduced neural network (HPNN), capable of learning the vast global PES data for elements across the periodic table. We show that the high-order spherical harmonics up to $l = 6$ are critical to describe complex PES, such as TiO_2 material low-concentration defects and chemical reactions. Instead of performing the CG tensor product operation, we introduce effective schemes to incorporate high-order spherical harmonics and achieve a linear spherical-harmonics-related computational complexity $O(2l)$ with balanced accuracy and speed performance. A generalized global neural network (GG-NN) potential with the HPNN architecture is obtained by training on a 5.8 million global PES dataset covering 83 elements (2025 August), which shows the great potential for structure and reaction prediction in general.

2 Methods

2.1 High-order pair-reduced neural network

Aiming to explore the global PES of molecules and materials in general, which contains a large number of structures with distorted/disordered configurations, we here develop an HPNN model, focusing on solving the high spatial discrimination between structures and achieving high-speed performance in PES computation. As illustrated in Figure 1, our HPNN model includes an input

sector to take structure information, an interaction block containing fixed three high-order pair-reduced (HP) layers to abstract molecular features, and a readout NN to obtain the energy of the system. HPNN follows the general scheme of GPU-based graph neural network models (Figure S1, Supporting Information online), but invents a new interaction layer to incorporate the neighboring information. Specifically, the HPNN does not utilize the message passing via CG tensor product, but includes different orders of spherical harmonics up to $l_{\max} = 6$ via concatenation. The HPNN architecture is now elaborated as follows.

In the input module, we represent each atom i in a system by a node vector of length N_n , $\mathbf{x}_i = \{x_i^k, k = 1, 2, \dots, N_n\}$. The node vector is initialized via an embedding layer with the element Z_i as input, as shown in Eq. (1). In the meantime, another embedding layer is utilized for each element to yield a scalar value, E_i^{ref} , the energy reference of the element, as shown in Eq. (2), which defines the energy baseline for the element. The introduction of E_i^{ref} can speed up the convergence of training markedly.

$$\mathbf{x}_i = \text{Embed}_v(Z_i) \quad (1)$$

$$E_i^{\text{ref}} = \text{Embed}_s(Z_i) \quad (2)$$

For the atomic pair within a preset cutoff r_{cut} (typically below 5 Å), we employ Gaussian functions (\mathbf{G}) to encode its distance r_{ij} into a pair vector, $\mathbf{RO}_{ij} = \{\text{RO}_{ij}^k, k = 1, 2, \dots, N_p\}$, of dimension N_p , as shown in Eqs. (3)–(5), where r_k is the center of the Gaussian function, incremental from 0 to r_{cut} , and σ is the Gaussian width. \mathbf{RO}_{ij} is then utilized as the input for a two-layer NN, the pair-NN, which outputs the pair vector \mathbf{R}_{ij} for use in the interaction blocks.

$$\text{RO}_{ij}^k = \mathbf{G}^k(r_{ij}) = \exp\left(-\frac{(r_{ij} - r_k)^2}{2\sigma^2}\right) \quad (3)$$

$$f_c(r_{ij}) = \begin{cases} 0.5 \times \tanh^3\left[1 - \frac{r_{ij}}{r_{\text{cut}}}\right], & \text{for } r_{ij} \leq r_{\text{cut}} \\ 0, & \text{for } r_{ij} > r_{\text{cut}} \end{cases} \quad (4)$$

$$\mathbf{R}_{ij} = \text{NN}\{\mathbf{RO}_{ij}\} \cdot f_c(r_{ij}) \quad (5)$$

2.1.1 Interaction block

The interaction block performs the message passing to update the node vector \mathbf{x}_i . The message passing is pair-based by exploiting the geometrical information of atomic pairs, including the pair vector \mathbf{R}_{ij} and the spherical function $Y^{lm}(\mathbf{r}_{ij})$. The interaction block is constituted by three HP layers, each containing a pair-based message passing followed by an atom-based two-layer NN. Compared to EGNN, the interaction block of HPNN, as shown in Figure 1b, has two major improvements implemented to balance the high efficiency and good accuracy.

First, considering the high computational load of the pair operation in message passing, particularly in solid materials with many neighbors, we shrink the dimension of atomic features \mathbf{x}_i to \mathbf{p}_i with a shrinking linear layer upon entering the interaction block (see Eq. (6)), but restore the dimension to \mathbf{x}_i with an expanding linear layer once the pair operation is finished. In this way, the parameter space of HPNN will not be compromised at the expense of the pair operation since the subsequent atomic NN remains to operate at the full dimension \mathbf{x}_i . In practice, \mathbf{p}_i can be half or even a quarter of the original \mathbf{x}_i .

$$\mathbf{p}_i = \mathbf{W}^1 \mathbf{x}_i + \mathbf{b} \quad (6)$$

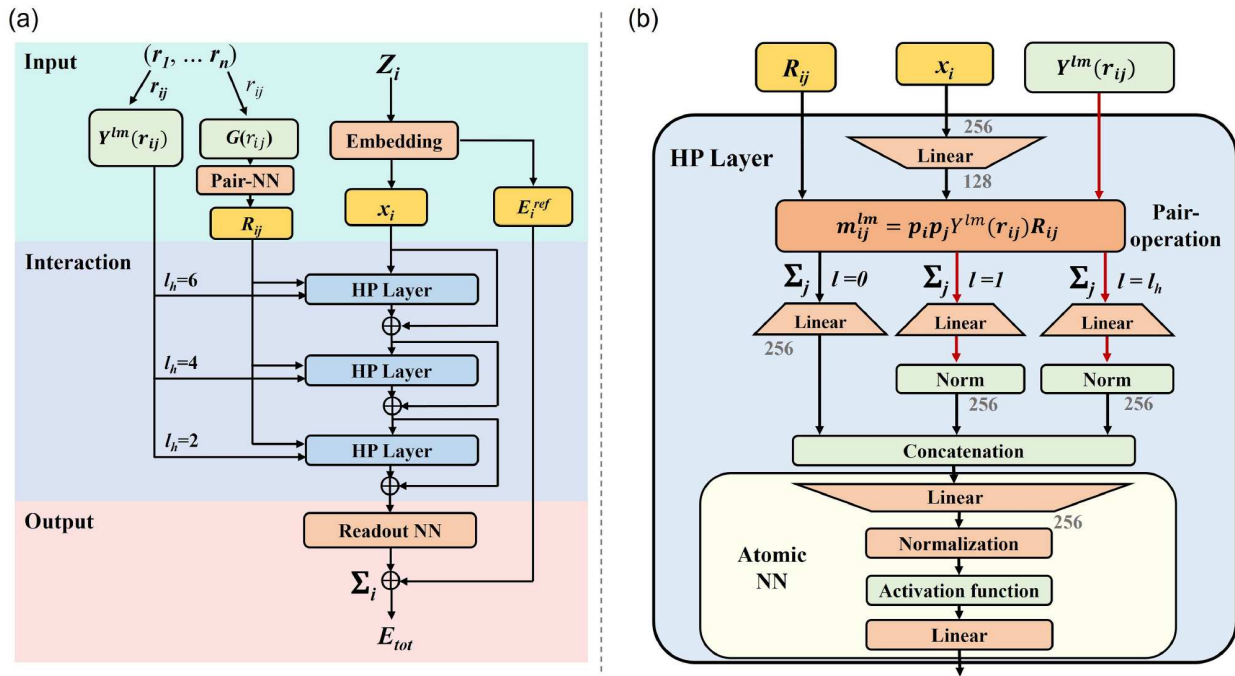


Figure 1 (Color online) Architecture of the HPNN. (a) Overall scheme of HPNN. The model takes atomic numbers Z_i and 3D coordinates $(\mathbf{r}_1, \mathbf{r}_2, \dots, \mathbf{r}_n)$ as inputs, and outputs the total energy (E_{tot}) of the structure. (b) Illustration of the HP interaction layer, which realizes the separated messaging passing at various l orders, couples spherical harmonics of various orders into atomic features that pass atomic NN with layer normalization and activation.

Second, as the CG tensor product is highly computationally intensive, which practically prevents the use of the high-order spherical functions, we adopt a variable angular interaction scheme to incorporate high-order angular information hierarchically with l_{max} up to 6. The message in HPNN is formulated in Eqs. (7) and (8),

$$\mathbf{m}_{ij}^{lm} = (\mathbf{p}_i \odot \mathbf{p}_j \odot \mathbf{R}_{ij}) \otimes Y^{lm}(\mathbf{r}_{ij}) \quad (7)$$

$$\mathbf{e}_i^l = \left\| W^l \sum_{j=1}^{\text{Nei}} \mathbf{m}_{ij}^{lm} \right\|_2, \quad (l = 0, 1, l_h) \quad (8)$$

$$\mathbf{x}_i^{t+1} = \mathbf{x}_i^t + \text{NN}(\mathbf{e}_i^0 \oplus \mathbf{e}_i^1 \oplus \mathbf{e}_i^{l_h}) \quad (9)$$

where the message \mathbf{m}_{ij}^{lm} is now written as the Hadamard product of the shrunk atomic features, followed by the outer product with individual spherical harmonics of different orders. In each HP layer, we simultaneously perform $l = 0, l = 1$, and $l = l_h$. Eq. (8) transforms aggregated angular messages into a scalar representation \mathbf{e}_i^l within each HP layer by computing the magnitude of the spherical harmonic. The angular-dependent atomic features \mathbf{e}_i^l ($l = 0, 1, l_h$) are concatenated and pass the atomic NN (Eq. (9)) to yield the updated atomic feature \mathbf{x}_i^{t+1} . By stacking the HP interaction layer three times with a varied l_h , a hierarchical incorporation of high-order angular information is achieved. Specifically, the initial HP layer utilizes the spherical harmonic with $l_h = 6$ to encode the highest resolution angular details, focusing on the local geometry, while the latter two layers adopt gradually reduced order harmonics with $l_h = 4$ and $l_h = 2$, respectively, aggregating the non-local geometry information of the overall structure. This design is inspired by convolutional neural networks (CNNs) [48], where early layers extract fine-grained, high-frequency local patterns and later layers capture broader, smoother contextual information. In Table S1 (Supporting Information online), we show that the

hierarchical HP architecture with three layers (l_h being 6, 4, 2 consecutively) achieves the best performance in PES accuracy compared to other choices of l_h .

We emphasize that the HPNN architecture is a lightweight invariant model, where only node scalar information is iteratively updated in ResNet. It differs from the implementation in EGNN, where the vector components ($l > 0$) are preserved and updated throughout the interaction blocks but are eventually discarded before entering the output sector [42–45]. Our choice is, in fact, natural since only the total energy of the system, a scalar quantity, is to be predicted directly for the ML potential with the forces obtained by computing the derivatives of the total energy via network backpropagation.

2.1.2 Output

Similar to the previous ML models, a readout NN using three fully connected layers transforms the final atomic features \mathbf{x}_i from the interaction block into a scalar value, which represents the energy correction term of the atom in the chemical environment. The total energy of the system is then obtained by summing the energy correction terms together with all atomic E_i^{ref} energies from the input sector, as shown in Eq. (10).

$$E_{\text{tot}} = \sum_{i=1}^n \text{NN}(\mathbf{x}_i) + \sum_{i=1}^n E_i^{\text{ref}} \quad (10)$$

2.2 Inference efficiency of HPNN

To assess the performance of HPNN in PES evaluation, we performed a series of benchmark inference calculations, as shown in Figure 2a, on a TiO_2 bulk crystal with different numbers of atoms (96 to 8,160 atoms) using a single GPU (NVIDIA GeForce RTX 4090). The performance of HPNN (3 layers, $l_{\text{max}} = 6$) is compared with that of mainstream GPU models, *e.g.*, PaiNN model [40] (3 layers, $l_{\text{max}} = 1$), NequIP model [42] (3 layers, $l_{\text{max}} = 2$), Allegro

model [43] (3 layers, $l_{\max} = 2$), MACE model [44] (3 layers, $l_{\max} = 2$), and a more recent SO3KRATES model [45] (3 layers, $l_{\max} = 3$) with a similar parameter size (~ 1.4 M). These representative models' parameters and theoretical scaling with respect to key parameters (N_p , l_{\max}) are listed in Table 1. Our results are summarized in Figure 2a and Table S2. We found that for the smallest system of 96 atoms, the SO3KRATES model achieves the fastest inference efficiency, specifically 8.00 ms per energy/force evaluation. The PaiNN model with the lowest order also has a high inference efficiency of 11.92 ms, slightly outperforming HPNN (13.65 ms). All of these are significantly faster than MACE, which requires 53.61 ms for the same task (NequIP and Allegro have the same scaling as MACE; NequIP results shown in Table S2). As the system size increases, the inference time of the MACE model (green) grows rapidly, being the longest among all tested models (Figure 2a) until reaching the limit of 1,920 atoms, the largest size capable of fitting in a single RTX 4090 GPU due to excessive memory consumption of tensor product operations. In contrast, HPNN (blue), PaiNN (orange), and SO3KRATES (purple) exhibit a good linear scaling up to 8,500, with HPNN surpassing PaiNN beyond 96 atoms and SO3KRATES beyond 3,840 atoms, revealing its superior scalability for large-scale atomistic simulation. This performance is consistent with the scaling data of different models, as listed in Table 1, where both HPNN and SO3KRATES achieve a low scaling with respect to l_{\max} . It might be mentioned that the inference of the SO3KRATES model utilizes the more efficient JAX package [49], which is intrinsically faster than the PyTorch package [50,51] used in our HPNN.

Figure 2b compares the performance of the multi-GPU version of HPNN (four GPU devices utilized in the figure) with that of a single-GPU version, with all data detailed in Table S3. Two techniques

enabling HPNN to handle systems containing more than ten thousand atoms are also illustrated in Table S3. Although multi-GPU implementation incurs a higher latency due to the inter-GPU communication overhead (*e.g.*, 64.34 ms for small systems), its inference performance surpasses that of the single-GPU version beyond the system size of 4,800 atoms. The computation time scales linearly with the system size, the curve of which has a smaller slope compared to that in the single-GPU version, demonstrating high scalability towards large-scale atomic simulations. Impressively, at a medium size of 8,160 atoms, the multi-GPU version reduces the inference time by nearly 50% (97.01 ms vs. 201.71 ms for single-GPU).

Apart from the bulk Ti–O system, we also performed training and inference tests on an isolated system, *i.e.*, the Chignolin mini protein, where the efficiency tests of some mainstream ML potential models are available from the literature. Briefly, on the chignonin dataset, HPNN achieves a training time of 7.08 ms per structure on a single NVIDIA V100 GPU, which is significantly faster than other models (*e.g.*, MACE: 101.6 ms, NequIP: 233.6 ms) [46], and related data are detailed in Table S4. The HPNN model also exhibits a good inference latency, *i.e.*, 11.7 ms for energy and force calculations per structure (RTX 4090 GPU), which outperforms TensorNet [52] (26.5 ms) and ET [24] (26.8 ms) models. These results confirm the high speed and scalability of HPNN in both training and inference.

3 Results and discussion

With the high performance of the HPNN architecture, we established a generalized global neural network (GG-NN) potential, leveraging all the datasets of the LASP project [19–21] that were utilized to generate more than 340 G-NN potentials of the G-NN

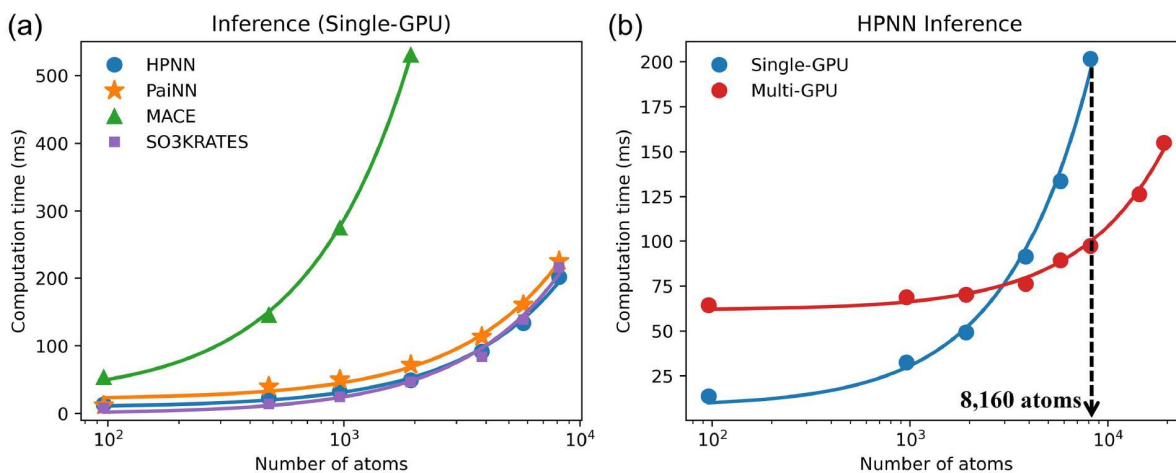


Figure 2 (Color online) Inference efficiency of HPNN on single and multi-GPU systems. (a) Single-GPU inference times for HPNN, MACE, and PaiNN on TiO₂ systems (96 to 8,160 atoms). See Table 1 for hyperparameters. For the MACE model, the cuEquivariance library is not utilized. (b) Inference times for single-GPU and multi-GPU (four cards) versions of HPNN.

Table 1 Hyperparameters and theoretical scaling of GPU-based ML potential models

Model	Params (M)	N_{sca}	N_{vec}	N_p	l_{\max}	N_{int}	Scaling ^{a)}
HPNN	1.51	256	0	128	6	3	$O(n \times N_{\text{ei}} \times (2l_{\max} + 5) \times N_p)$
PaiNN	1.40	196	196×3	196	1 [#]	3	$O(n \times N_{\text{ei}} \times 4 \times N_p)$
NequIP	1.44	64	64×8	64	2	3	$O(n \times N_{\text{ei}} \times (l_{\max} + 1)^6 \times N_p)$
Allegro	1.30	64	64×8	64	2	3	$O(n \times N_{\text{ei}} \times (l_{\max} + 1)^6 \times N_p)$
MACE	1.47	128	128×3	128	2	3	$O(n \times N_{\text{ei}} \times (l_{\max} + 1)^6 \times N_p)$
SO3KRATES	1.40	288	15	288	3	3	$O(n \times N_{\text{ei}} \times ((l_{\max} + 1)^2 + N_p))$

a) n is the number of atoms; N_{ei} is the number of neighbors; [#] PaiNN l_{\max} is fixed as 1 (Params: the number of model parameters, N_{sca} : scalar node feature length, N_{vec} : vector components node feature length, N_p : pair feature length, l_{\max} : maximum degree of spherical harmonics, N_{int} : the number of interaction layers). The cutoff radius for all listed models is the same, 5 Å.

library (<http://lasphub.com/#/lasphubLibrary>) for the LASP software in the past decade. In the following, we first present the GG-NN potential (Sect. 3.1) and benchmark the performance of the GG-NN potential and the specifically trained HPNN potential against other mainstream GPU models in the challenging global PES system, aiming to predict TiO_x solid energetics with low concentration defects (Sect. 3.2), and chemical reaction barriers of gas phase molecules (Table S8). The former one involves the long-range interaction ($>10 \text{ \AA}$) between low-content defects, and the latter one requires a high resolution to resolve the local geometry change during reaction. Both systems have been utilized previously to assess the performance of CPU-based LASP potentials [27,53]. In addition, to guide the practical use of GG-NN, we also illustrate the GG-NN performance in material prediction (Matbench [54]) in comparison with other universal foundation potential models (Sect. 3.3).

3.1 GG-NN potential

The dataset for the GG-NN potential comprises 5,844,031 unique configurations over 83 elements, as summarized in Figure 3a, covering the most common elements in the periodic table. The generation scheme and density functional theory (DFT) setup are detailed in Figure S2. It should be mentioned that the spin-polarization was taken into account for structures containing 3d elements (V, Cr, Mn, Fe, Co, Ni) and f-block lanthanide elements.

The final GG-NN potential exhibits good accuracy, namely, the root-mean-square errors (RMSE) of 7.348 meV/atom for energy, 0.163 eV/Å for atomic forces on the global training dataset. The levels of error are comparable to the CPU-based G-NN potentials utilized in the LASP project, which have been widely utilized by

many users [55–58]. These results demonstrate a good learning ability of the HPNN model for the vast global PES data across the periodic table. Our previous work [53] have shown that the PES prediction using global NN potential is generally robust, but extra data on the target PES is essential in order to reach a very high accuracy for the target system (such as $\sim 1 \text{ meV/atom}$), which can be achieved by re-training with expanded training data, or, more conveniently, by fine-tuning with newly-generated target PES dataset.

To give a quick outlook of GG-NN performance, Figure 3b, c shows the zero-shot performance of the GG-NN calculations, predictions without system-specific training, in two complex surface systems recently investigated by our group [59,60], namely, CO activation in Fischer-Tropsch synthesis on iron carbide surfaces and the adsorption of diverse organic molecules on copper surfaces. Both systems are covered by the training dataset, and thus, the purpose is to examine the GG-NN potential performance against the previously published CPU-based G-NN potentials trained specifically on the target systems.

As shown in Figure 3b, the GPU-based GG-NN potential predicts well the reaction pathway energetics for CO activation on the Fe_5C_2 (510) surface [61]. The mean absolute error (MAE) in the predicted Gibbs free energy along the pathway is 0.0501 eV compared to the DFT data, while our previous CPU-based G-NN potential has an MAE of 0.0768 eV. Detailed Gibbs free energies of initial, transition, and final states are provided in Table S5. For molecular adsorption on Cu surfaces [62], as shown in Figure 3c, we examined 10,000 molecules and fragments with unique functional group configurations adsorbed on three low-index Cu surfaces: (111), (100), and (211). The composition distribution of these organic molecules and fragments is shown in Figure S3. The GPU-based GG-NN potential

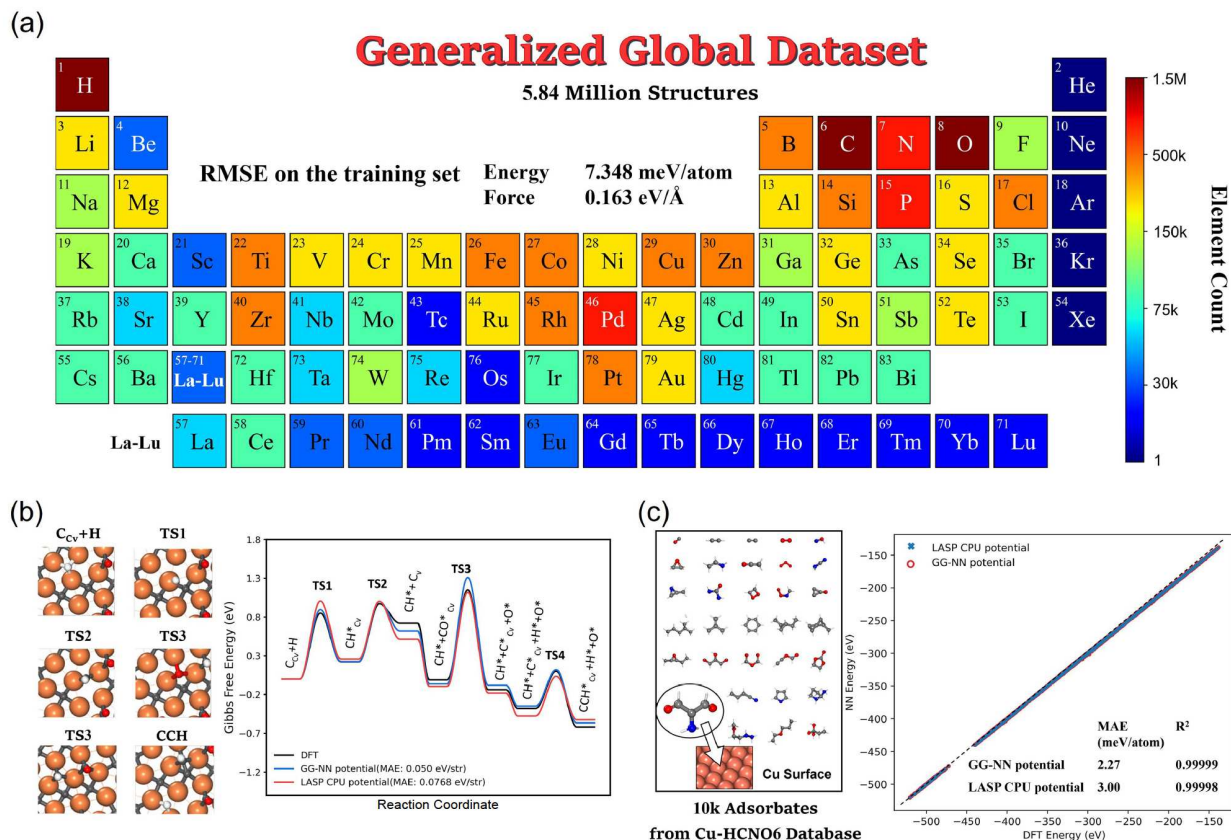


Figure 3 (Color online) Generation and Performance of GG-NN. (a) Element distribution of generalized global datasets and RMSE accuracy of GG-NN potential. (b) Performance of GG-NN potential in predicting CO activation in Fischer-Tropsch synthesis on the Fe_5C_2 (510) surface. (c) Performance of the GG-NN potential in predicting the energies of 10,000 different organic molecules adsorbed on Cu surfaces. The atomic elements are color-coded as follows: C in grey, H in white, O in red, Fe in orange, N in blue, and Cu in coral.

achieves an MAE of 2.27 meV/atom for the energies of these adsorbed structures and an R^2 coefficient near 1 (0.99999), compared to 3.00 meV/atom and 0.99998 for the CPU-based G-NN potential. These two examples demonstrate the good agreement among GG-NN, CPU-based G-NN, and DFT calculations, and confirm a robust performance of GG-NN across different surfaces and molecular configurations. Considering the vast global PES data across the periodic table can now be learned into one model with only 1.5 million parameters, the GG-NN-based atomic simulation offers a convenient and unified platform to handle different PES problems.

Apart from that, we performed MD simulations to examine the GG-NN model's numerical stability on evaluating the kinetics of two example systems, namely the anatase $\text{TiO}_2(101)$ surface [53], and the water droplet on quartz $\alpha\text{-SiO}_2(110)$, a large system with 8,541 atoms, which are detailed in Figure S4. For the anatase $\text{TiO}_2(101)$ surface, the GG-NN predictions exhibit excellent agreement with reference DFT calculations, achieving an RMSE of relative energy as low as 1.70 meV/atom. For the water droplet, the GG-NN model maintains stable dynamics over long simulation times, *i.e.*, max energy deviation is 0.045 meV/atom, further demonstrating its robustness in handling large and complex systems.

3.2 Global PES of Ti–O binary systems

We then evaluated the performance of the GG-NN and specifically-trained HPNN model on two challenging systems. The first example

is the Ti–O binary global PES [63]. This dataset includes 27,278 global PES structures with various chemical compositions ranging from gas molecules to surface slabs and to bulk structures, including 6,187 Ti, 13,026 TiO_2 , 6,820 TiO_{2-x} , 664 O_2 , and 581 $\text{Ti}_{1-x}\text{O}_2$ structures in chemical formula. The TiO_{2-x} and $\text{Ti}_{1-x}\text{O}_2$ structures are mostly defective TiO_2 bulk crystals with O and Ti vacancies, respectively. Structural details, including chemical formulas, atom counts, and structure types (cluster, bulk, layer), are provided in Table S6. The complexity of the Ti–O global dataset can be visualized in Figure 4a, where the x - and y -axes denote the distance-weighted Steinhardt order parameters (OP_2 and OP_4) [64], two different structural descriptors, and the z -axis represents the relative energy with respect to the stable elemental structures of Ti and O. It shows that the energy of the structures spans a wide range, from -1 to 6 eV/atom, with the stable structures, *e.g.*, Ti crystal bulk, O_2 , and TiO_2 crystal, located at the bottom, and the configurations, *e.g.*, Ti clusters, defective $\text{Ti}_{1-x}\text{O}_2$, and TiO_{2-x} clusters at high-energy regions.

The HPNN and other mainstream GPU models, including PaiNN, NequIP, Allegro, and MACE, were then trained on the same Ti–O global dataset with a randomly split train and test sets at a 95% to 5% ratio. The number of parameters for each model and the maximum order of spherical harmonics (l_{\max}) are summarized in Table 1. Figure 4b displays the performance of the different models. Performance and architectural details are provided in Table S7. Notably, our HPNN model ($l_{\max} = 6$) shows the best performance in terms of energy and force errors on the Ti–O test dataset, with RMSE

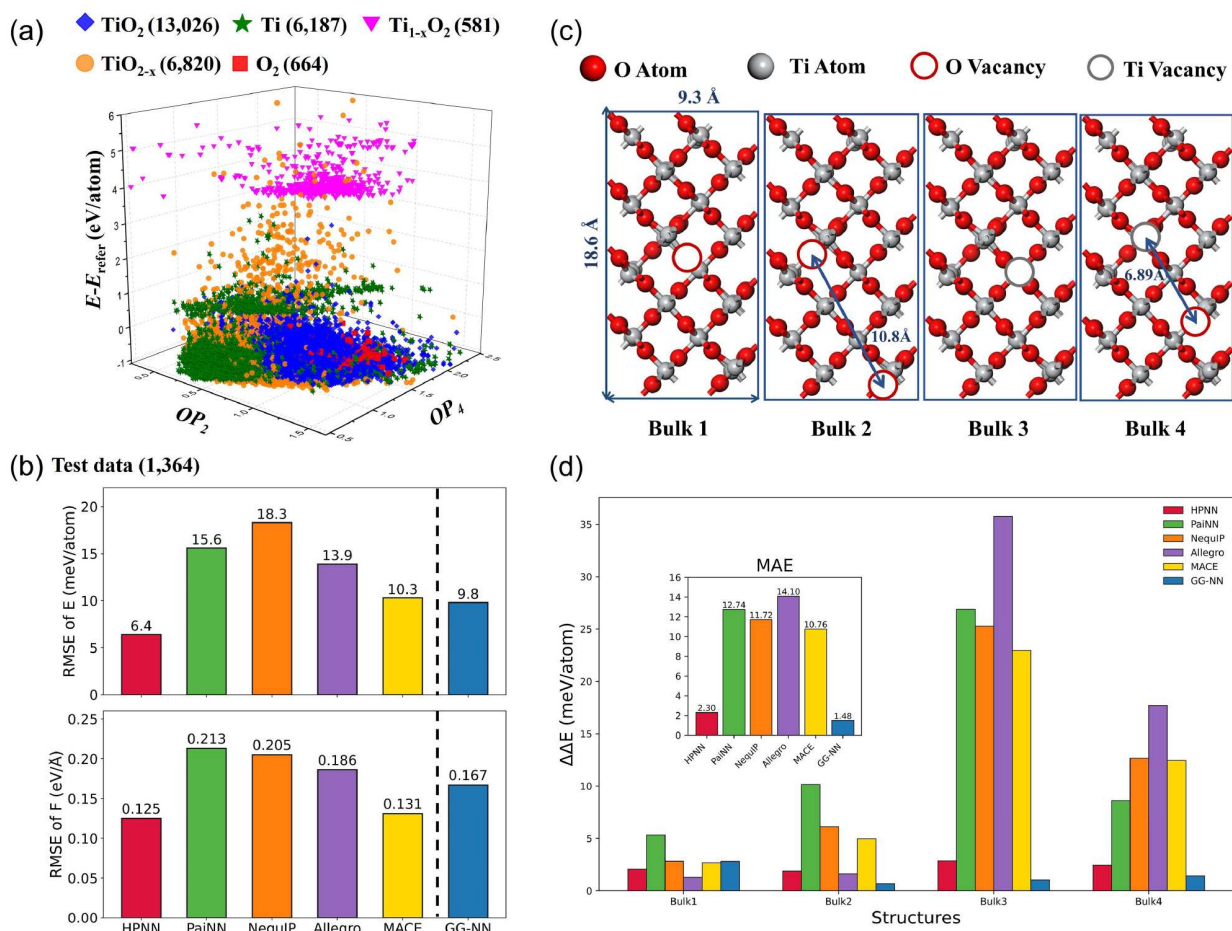


Figure 4 (Color online) Ti–O Global PES and Model Performance. (a) Distribution of the Ti–O global dataset (including O_2 , Ti, TiO_2 , TiO_{2-x} , and $\text{Ti}_{1-x}\text{O}_2$). The x - and y -axes represent Steinhardt order parameters (OP_2 , OP_4), and the z -axis shows relative energy relative to the reference values for the Ti crystal and the O_2 molecule. (b) Performance comparison of HPNN, PaiNN, NequIP, Allegro, MACE, and GG-NN on the test set, including errors in energy and forces. See Table 1 for hyperparameters. (c) Four defective TiO_2 (rutile) structures. (d) The error in predicting vacancy formation energy ($\Delta\Delta E$) by HPNN, PaiNN, NequIP, Allegro, MACE, and GG-NN on the defective bulk structures in reference to DFT values.

of 6.4 meV for energy and 0.125 eV/Å for forces. The MACE model, which employs CG tensor product and the spherical harmonics $l_{\max} = 2$, ranks second with RMSE values of 10.3 meV for energy and 0.131 eV/Å for forces, where the force accuracy approaches HPNN's force accuracy. The PaiNN model and NequIP model perform relatively poorly, with RMSE values of 15.6 meV/atom and 0.213 eV/Å for PaiNN, and 18.3 meV/atom and 0.205 eV/Å for NequIP, primarily due to PaiNN's limited spherical harmonic order ($l_{\max} = 1$) and NequIP's lower atomic feature dimensions (64 per order). Meanwhile, Allegro, incorporating two-body energy terms, outperforms both PaiNN and NequIP with RMSE values of 13.9 meV/atom for energy and 0.186 eV/Å for forces, though it remains less accurate than MACE. We also note that the zero-shot GG-NN performs better than PaiNN, NequIP, Allegro models, and is slightly worse than MACE in the force prediction. This is encouraging, considering that no extra training is required to utilize the generalized potential.

Considering that defective sites in oxides, such as oxygen vacancies, play a crucial role in determining material properties, we also assessed the predictive ability of different models in calculating the defect formation energy (ΔE) of defective TiO₂ systems. We constructed defective structures based on a 192-atom rutile TiO₂ crystal by systematically removing oxygen (O) or titanium (Ti) atoms, as shown in Figure 4c. Bulk-1 is the bulk structure with a single O defect, Bulk-2 has double O defects, Bulk-3 contains a single Ti defect, and Bulk-4 has one O vacancy and one Ti vacancy. The performance of various models in predicting the defect formation energy error ($\Delta\Delta E$) for defective TiO₂ structures with respect to DFT results is summarized in Figure 4d.

Again, our HPNN model achieves the best accuracy across defective structures (bulk-1 to bulk-4), with a defect formation energy error of less than 5 meV/atom. In contrast, PaiNN, NequIP, Allegro, and MACE exhibit higher errors, particularly on Ti vacancy structures (bulk-3 and bulk-4), where their error is greater than 10 meV/atom. This suggests the high-order spherical functions are critical in capturing the cation vacancy-associated long-range interactions. It is interesting to note that the zero-shot GG-NN outperforms in this test case, with the best performance in $\Delta\Delta E$ across Bulk-2, Bulk-3, and Bulk-4, which could be due to the success of transfer learning in the large dataset, where cation vacancies are well represented in structures containing other elements. We should emphasize that although the cutoff radius in HPNN is not large, being 5 Å, the non-local effect can be enveloped

via the stacking of three HP layers, leading to an overall perception range of 15 Å, which is enough for the TiO₂ example. If the defect concentration is further reduced, we expect that the vacancy formation energetics would be difficult to predict, even for HPNN.

3.3 Material prediction in matbench

It would be interesting to further compare our GG-NN model with other universal foundation potential models. For this purpose, we chose the Matbench Discovery leaderboard [61] that was established as a test of a model's ability for the high-throughput discovery of stable inorganic crystals. Since the training dataset utilized in generating GG-NN is different from the open-source dataset (*e.g.*, DFT calculation setup, Periodic Table element types), we have to retrain our GG-NN using the MPtrj dataset (1.58 M data) to cover 89 elements and rescale to the new energy scale of MPtrj. The performance benchmark on the WBM test set [62] (0.26 M) is thus finally obtained for the MPtrj-retrained GG-NN.

Figure 5a summarizes the MAE (x -axis in the figure), R^2 (color of the circle), and RMSD (y -axis in the figure) results for GG-NN and other top-performance models [54,65–73]. MAE and R^2 are from single-point energy calculations in evaluating the formation energy of crystals by comparing ML potential with DFT results, and RMSD measures the difference between the ML potential optimized structure and the DFT optimized structure, also recommended in the Matbench Discovery leaderboard. Our GG-NN results are as follows: MAE is 0.041, R^2 is 0.832, and RMSD is 0.056. Figure 5a shows that it is generally true that the larger the model (the size of the circle) is, the better the performance (the left-bottom of the figure) would be: the largest model, eSEN-30M-MP (30.2 M parameters), achieves the impressive performance in MAE (0.018) and the top RMSD (0.061). The energy performance (MAE) of GG-NN is comparable with other models that have a similar parameter size, including SevenNet-13i5 (1.17 M) and Eqnorm MPtrj (1.31 M), but, interestingly, the geometry (RMSD) from GG-NN ranks the best among them, which might be due to the fact that our GG-NN is a retrained model that inherits the knowledge from the global PES dataset.

Apart from the energetics and geometrical accuracy, we also compared the inference efficiency of GG-NN with other open-source universal foundation models at the comparable parameter size, namely SevenNet-13i5 and MACE-MP-0 (small and medium), using the same system and a single GPU (NVIDIA GeForce RTX 4090) as

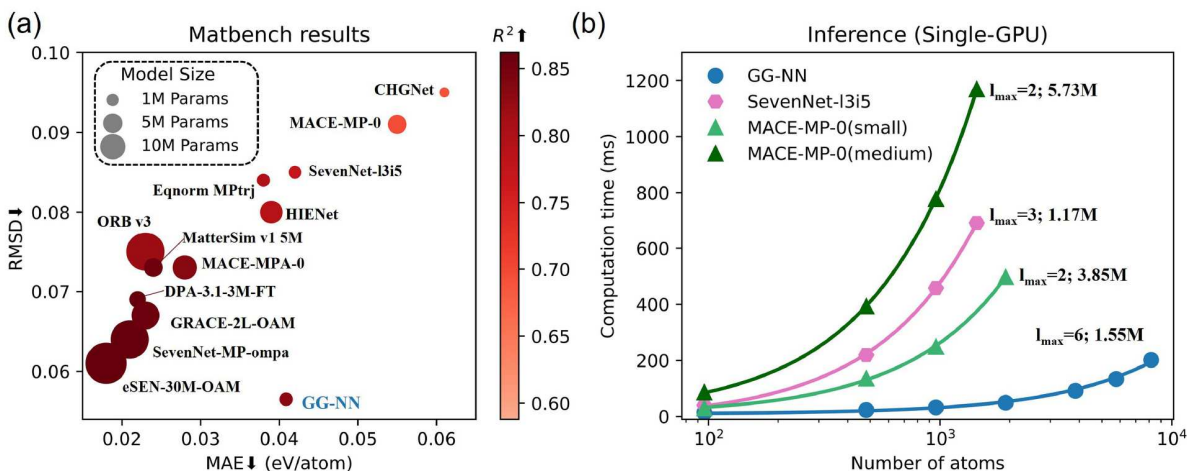


Figure 5 (Color online) Benchmarks of GG-NN with other universal foundation models. (a) Matbench results (MAE, RMSD, and R^2) for GG-NN and some representative models from the Matbench Discovery leaderboard on the WBM test set. The circle size indicates the number of parameters and (\uparrow/\downarrow) stands for the higher/lower, the better the model. (b) Inference efficiency of GG-NN compared with three universal foundation models (SevenNet-13i5, MACE-MP-0) on a single GPU (RTX 4090).

described in Sect. 2.2. SevenNet-I3i5 with $l_{\max} = 3$ has a similar parameter size (1.17 M) as GG-NN; MACE-MP-0 has two versions available, small ($l_{\max} = 2$, 3.85 M parameters) and medium ($l_{\max} = 2$, 5.73 M parameters). Figure 5b shows that GG-NN exhibits the best performance, maintaining the lowest scaling across different system sizes. Remarkably, the runtime of GG-NN for systems with $\sim 9,600$ atoms is comparable to that of other universal foundation models for systems with only a few hundred atoms, which allows GG-NN to be used directly for the production of large-scale atomic simulations. The inference efficiency on multiple GPUs for SevenNet-I3i5 and GG-NN is also compared, where the literature runtime is available. As shown in Table S9, SevenNet-I3i5 can only reach 8,160 atoms due to the memory limit on four GPU cards, taking 1,083.56 ms, whilst GG-NN costs only 201.55 ms to evaluate the same 8,160-atom structure.

4 Conclusions

This work proposes a low-cost and high-accuracy ML potential framework, namely HPNN, to learn the vast global PES across the periodic table. The HPNN features a hierarchical atom interaction scheme with reduced pair dimension that enables the incorporation of spherical harmonics up to $l = 6$ without sacrificing the computation speed. Using the HPNN architecture, a GG-NN potential with 1.5 M parameters is obtained by training an extensive dataset of 5.84 M global PES structures spanning 83 elements across the periodic table, which is ready for generalized global PES exploration.

We show that the GG-NN achieves a high speed in the inference and a high accuracy comparable to previous CPU-based G-NN potentials specifically trained for Fischer-Tropsch reactions on iron-carbide surface and molecular adsorption on metal surfaces. The performance of GG-NN is also benchmarked against HPNN and other mainstream ML potentials (*e.g.*, PaiNN and MACE) specifically trained in two systems, which shows that zero-shot GG-NN reaches an accuracy level comparable to specifically-trained potentials, while the specifically-trained HPNN outperforms all other models. By further benchmarking with other top-performance universal foundation models using Matbench, we demonstrate that GG-NN is among the top-ranked models and, importantly, being a fast, lightweight, gradient-based-force model, can be directly utilized for large-scale atomic simulations.

Conflict of interest

The authors declare no conflict of interest.

Acknowledgement

This work was supported by the National Key Research and Development Program of China (2024YFA1509600), the National Natural Science Foundation of China (12188101, 22033003, 92472113), the Fundamental Research Funds for the Central Universities (20720250005, 20720220011), the Science & Technology Commission of Shanghai Municipality (2024ZDSYS02), the Robotic AI-Scientist Platform of Chinese Academy of Sciences and the Tencent Foundation for XPLORER PRIZE. The computations in this research were performed using the CFFF platform of Fudan University.

Supporting information

The supporting information is available online at <http://chem.scichina.com> and <http://link.springer.com/journal/11426>. The supporting materials are published as submitted, without typesetting or editing. The responsibility for scientific accuracy and content remains entirely with the authors.

References

- Rupp M, Tkatchenko A, Müller KR, von Lilienfeld OA. *Phys Rev Lett*, 2012, 108: 058301
- Bartók AP, Payne MC, Kondor R, Csányi G. *Phys Rev Lett*, 2010, 104: 136403
- Behler J, Parrinello M. *Phys Rev Lett*, 2007, 98: 146401
- Bartók AP, Kondor R, Csányi G. *Phys Rev B*, 2013, 87: 184115
- Shi YF, Yang ZX, Ma S, Kang PL, Shang C, Hu P, Liu ZP. *Engineering*, 2023, 27: 70–83
- Unke OT, Chmiela S, Sauceda HE, Gastegger M, Poltavsky I, Schütt KT, Tkatchenko A, Müller KR. *Chem Rev*, 2021, 121: 10142–10186

- Zhang Y, Xia J, Jiang B. *Phys Rev Lett*, 2021, 127: 156002
- Gastegger M, Behler J, Marquetand P. *Chem Sci*, 2017, 8: 6924–6935
- Eastman P, Galvelis R, Peláez RP, Abreu CRA, Farr SE, Gallicchio E, Gorenko A, Henry MM, Hu F, Huang J, Krämer A, Michel J, Mitchell JA, Pande VS, Rodrigues JP, Rodriguez-Guerra J, Simmonett AC, Singh S, Swails J, Turner P, Wang Y, Zhang I, Chodera JD, De Fabritiis G, Markland TE. *J Phys Chem B*, 2023, 128: 109–116
- Li Z, Kermodé JR, De Vita A. *Phys Rev Lett*, 2015, 114: 096405
- Huang SD, Shang C, Kang PL, Liu ZP. *Chem Sci*, 2018, 9: 8644–8655
- Kang PL, Shang C, Liu ZP. *J Am Chem Soc*, 2019, 141: 20525–20536
- Liu QY, Shang C, Liu ZP. *J Am Chem Soc*, 2021, 143: 11109–11120
- Zhang L, Han J, Wang H, Car R, E W. *Phys Rev Lett*, 2018, 120: 143001
- Fu X, Wu Z, Wang W, Xie T, Keten S, Gomez-Bombarelli R, Jaakkola T. arXiv: 2210.07237
- Kang PL, Shang C, Liu ZP. *Acc Chem Res*, 2020, 53: 2119–2129
- Musil F, Grisafi A, Bartók AP, Ortner C, Csányi G, Ceriotti M. *Chem Rev*, 2021, 121: 9759–9815
- Huang SD, Shang C, Zhang XJ, Liu ZP. *Chem Sci*, 2017, 8: 6327–6337
- Kang P, Shang C, Liu Z. *Chin J Chem Phys*, 2021, 34: 583–590
- Xie XT, Yang ZX, Chen D, Shi YF, Kang PL, Ma S, Li YF, Shang C, Liu ZP. *Precision Chem*, 2024, 2: 612–627
- Huang S, Shang C, Kang P, Zhang X, Liu Z. *Wires Comput Mol Sci*, 2019, 9: e1415
- Schütt KT, Sauceda HE, Kindermans PJ, Tkatchenko A, Müller KR. *J Chem Phys*, 2018, 148: 241722
- Schütt KT, Arbabzadah F, Chmiela S, Müller KR, Tkatchenko A. *Nat Commun*, 2017, 8: 13890
- Liao Y-L, Smidt T. Equiformer: Equivariant graph attention transformer for 3D atomistic graphs. In: *Proceedings of the Eleventh International Conference on Learning Representations*. Kigali, 2023
- Reiser P, Neubert M, Eberhard A, Torresi L, Zhou C, Shao C, Metni H, van Hoesel C, Schopmans H, Sommer T, Friederich P. *Commun Mater*, 2022, 3: 93
- Zhang Y, Xia J, Jiang B. *J Chem Phys*, 2022, 156: 114801
- Kang PL, Yang ZX, Shang C, Liu ZP. *J Chem Theor Comput*, 2023, 19: 7972–7981
- Zhang Y, Hu C, Jiang B. *J Phys Chem Lett*, 2019, 10: 4962–4967
- Gilmer J, Schoenholz SS, Riley PF, Vinyals O, Dahl GE. Neural message passing for quantum chemistry. In: *Proceedings of the 34th International conference on machine learning*. Sydney: JMLR, 2017. 1263–1272
- Gasteiger J, Groß J, Günnemann S. Directional message passing for molecular graphs. In: *Proceedings of the International Conference on Learning Representations*. Addis Ababa, 2020
- Liu Y, Wang L, Liu M, Zhang X, Oztekin B, Ji S. Spherical message passing for 3D molecular graphs. In: *Proceedings of the International Conference on Learning Representations*. 2021
- Wang L, Liu Y, Lin Y, Liu H, Ji S. ComENet: Towards complete and efficient message passing for 3D molecular graphs. In: *Proceedings of the Advances in Neural Information Processing Systems*. New Orleans, 2022. 650–664
- Gasteiger J, Becker F, Günnemann S. GemNet: Universal directional graph neural networks for molecules. In: *Proceedings of the 35th International Conference on Neural Information Processing System*. Red Hook: Curran Associates Inc., 2021. 6790–6802
- Chmiela S, Sauceda HE, Müller KR, Tkatchenko A. *Nat Commun*, 2018, 9: 3887
- Christensen AS, Bratholm LA, Faber FA, Anatole von Lilienfeld O. *J Chem Phys*, 2020, 152: 044107
- Du W, Du Y, Wang L, Feng D, Wang G, Ji S, Gomes CP, Ma ZM. *Adv Neural Inf Process Syst*, 2023, 36: 66647–66674
- Drautz R. *Phys Rev B*, 2019, 99: 014104
- De S, Bartók AP, Csányi G, Ceriotti M. *Phys Chem Chem Phys*, 2016, 18: 13754–13769
- Satorras VG, Hoogeboom E, Welling M. $E(n)$ equivariant graph neural networks. In: *Proceedings of the International Conference on Machine Learning*. PMLR, 2021. 9323–9332
- Schütt KT, Unke OT, Gastegger M. Equivariant message passing for the prediction of tensorial properties and molecular spectra. In: *Proceedings of the International Conference on Machine Learning*. 2021
- Thomas N, Smidt T, Kearnes S, Yang L, Li L, Kohlhoff K, Riley P. arXiv: 1802.08219
- Batzner S, Musaelian A, Sun L, Geiger M, Mailoa JP, Kornbluth M, Molinari N, Smidt TE, Kozinsky B. *Nat Commun*, 2022, 13: 2453
- Musaelian A, Batzner S, Johansson A, Sun L, Owen CJ, Kornbluth M, Kozinsky B. *Nat Commun*, 2023, 14: 579
- Batatia I, Kovacs DP, Simm G, Ortner C, Csányi G. MACE: Higher order equivariant message passing neural networks for fast and accurate force fields. In: *Proceedings of the Advances in Neural Information Processing Systems*. New Orleans, 2022. 11423–11436
- Frank JT, Unke OT, Müller KR, Chmiela S. *Nat Commun*, 2024, 15: 6539
- Wang Y, Wang T, Li S, He X, Li M, Wang Z, Zheng N, Shao B, Liu TY. *Nat Commun*, 2024, 15: 313
- Passaro S, Zitnick CL. Reducing SO(3) convolutions to SO(2) for efficient equivariant GNNs. In: *Proceedings of the 40th International Conference on Machine Learning*. Honolulu, 2023. 27420–27438
- Duvenaud D, Maclaurin D, Aguilera-Iparraguirre J, Gómez-Bombarelli R, Hirzel T,

- Aspuru-Guzik A, Adams RP. Convolutional networks on graphs for learning molecular fingerprints. In: *Proceedings of the 29th International Conference on Neural Information Processing Systems*. Montreal, 2015
- 49 Bradbury J, Frostig R, Hawkins P, Johnson MJ, Leary C, Maclaurin D, Wanderman-Milne S. JAX: Composable transformations of Python+NumPy programs. 2018
- 50 Paszke A, Gross S, Massa F, Lerer A, Bradbury J, Chanan G, Killeen T, Lin Z, Gimelshein N, Antiga L, Desmaison A, Köpf A, Yang E, DeVito Z, Raison M, Tejani A, Chilamkurthy S, Steiner B, Fang L, Bai J, Chintala S. PyTorch: An imperative style, high-performance deep learning library. In: *Proceedings of the Advances in Neural Information Processing Systems*. Vancouver: Curran Associates Inc., 2019
- 51 Bafghi RA, Raissi M. Comparing PINNs across frameworks: JAX, TensorFlow, and PyTorch. In: *Proceedings of the ICLR 2024 Workshop on AI4 Differential Equations in Science*. Vienna, 2024
- 52 Simeon G, de Fabritiis G. arXiv: 2306.06482
- 53 Xie XT, Guan T, Yang ZX, Shang C, Liu ZP. *J Chem Theor Comput*, 2025, 21: 3576–3586
- 54 Deng B, Zhong P, Jun KJ, Riebesell J, Han K, Bartel CJ, Ceder G. *Nat Mach Intell*, 2023, 5: 1031–1041
- 55 Shi YF, Kang PL, Shang C, Liu ZP. *J Am Chem Soc*, 2022, 144: 13401–13414
- 56 Zhang KX, Chen L, Liu ZP. *J Am Chem Soc*, 2024, 146: 35416–35426
- 57 Chen D, Chen L, Zhao QC, Yang ZX, Shang C, Liu ZP. *Nat Catal*, 2024, 7: 536–545
- 58 Wang M, Zhang S, Gong Y, Zhang W, Wang Y, Chen Y, Zheng Q, Liu Z, Tang C. *Angew Chem Int Ed*, 2024, 63: e202409283
- 59 Liu QY, Chen D, Shang C, Liu ZP. *Chem Sci*, 2023, 14: 9461–9475
- 60 Guo ZX, Song GL, Liu ZP. *Chem Sci*, 2024, 15: 13369–13380
- 61 Riebesell J, Goodall REA, Benner P, Chiang Y, Deng B, Ceder G, Asta M, Lee AA, Jain A, Persson KA. *Nat Mach Intell*, 2025, 7: 836–847
- 62 Wang HC, Botti S, Marques MAL. *npj Comput Mater*, 2021, 7: 12
- 63 Ma S, Huang SD, Fang YH, Liu ZP. *ACS Catal*, 2018, 8: 9711–9721
- 64 Steinhardt PJ, Nelson DR, Ronchetti M. *Phys Rev B*, 1983, 28: 784–805
- 65 Fu X, Wood BM, Barroso-Luque L, Levine DS, Gao M, Dzamba M, Zitnick CL. arXiv: 2502.12147
- 66 Rhodes B, Vandenhoute S, Šimkus V, Gin J, Godwin J, Duignan T, Neumann M. arXiv: 2504.06231
- 67 Kim J, Kim J, Kim J, Lee J, Park Y, Kang Y, Han S. *J Am Chem Soc*, 2025, 147: 1042–1054
- 68 Bochkarev A, Lysogorskiy Y, Drautz R. *Phys Rev X*, 2024, 14: 021036
- 69 Zhang D, Peng A, Cai C, Li W, Zhou Y, Zeng J, Guo M, Zhang C, Li B, Jiang H, Zhu T, Jia W, Zhang L, Wang H. arXiv: 2506.01686
- 70 Batatia I, Benner P, Chiang Y, Elena AM, Kovács DP, Riebesell J, Advincula XR, Asta M, Avaylon M, Baldwin WJ, Berger F, Bernstein N, Bhowmik A, Bigi F, Blau SM, Cărare V, Ceriotti M, Chong S, Darby JP, De S, Pia FD, Deringer VL, Elijošius R, El-Machachi Z, Falcioni F, Fako E, Ferrari AC, Gardner JLA, Gawkowski MJ, Genreith-Schriever A, George J, Goodall REA, Grandel J, Grey CP, Grigorev P, Han S, Handley W, Heenen HH, Hermansson K, Holm C, Ho CH, Hofmann S, Jaafar J, Jakob KS, Jung H, Kapil V, Kaplan AD, Karimitari N, Kermode JR, Kourtis P, Kroupa N, Kullgren J, Kuner MC, Kuryla D, Liepuoniute G, Lin C, Margraf JT, Magdäu IB, Michaelides A, Moore JH, Naik AA, Niblett SP, Norwood SW, O'Neill N, Ortner C, Persson KA, Reuter K, Rosen AS, Rosset LAM, Schaaf LL, Schran C, Shi BX, Sivonxay E, Stenczel TK, Svahn V, Sutton C, Swinburne TD, Tilly J, van der Oord C, Vargas S, Varga-Umbrich E, Vegge T, Vondrák M, Wang Y, Witt WC, Wolf T, Zills F, Csányi G. arXiv: 2401.00096
- 71 Yang H, Hu C, Zhou Y, Liu X, Shi Y, Li J, Li G, Chen Z, Chen S, Zeni C, Horton M, Pinsler R, Fowler A, Zügner D, Xie T, Smith J, Sun L, Wang Q, Kong L, Liu C, Hao H, Lu Z. arXiv: 2405.04967
- 72 Yan K, Bohde M, Kryvenko A, Xiang Z, Zhao K, Zhu S, Kolachina S, Sarıtürk D, Xie J, Arroyave R, Qian X, Qian X, Ji S. arXiv: 2503.05771
- 73 Park Y, Kim J, Hwang S, Han S. *J Chem Theor Comput*, 2024, 20: 4857–4868